

Lawrence Berkeley National Laboratory

LBL Publications

Title

Rare-Earth Permanent Magnet SmCo₅ for Chiral Interfacial Spin-Orbitronics

Permalink

<https://escholarship.org/uc/item/2cd4f266>

Journal

Advanced Functional Materials, 31(46)

ISSN

1616-301X

Authors

Zhou, Heng-An
Liu, Jiahao
Wang, Zidong
[et al.](#)

Publication Date

2021-11-01

DOI

10.1002/adfm.202104426

Peer reviewed

Rare-earth permanent magnet SmCo_5
for chiral interfacial spin-orbitronics

Heng-An Zhou^{1,2,*}, Jiahao Liu^{1,2,3,*}, Zidong Wang^{1,2}, Qihan Zhang^{1,2}, Teng Xu^{1,2},
Yiqing Dong^{1,2}, Le Zhao^{1,2}, Soong-Geun Je^{4,5}, Mi-Young Im⁴, [Kun Xu⁶](#), [Jing Zhu⁶](#) and
WanJun Jiang^{1,2,†}

¹State Key Laboratory of Low-Dimensional Quantum Physics and Department of Physics, Tsinghua University, Beijing 100084, China

²Frontier Science Center for Quantum Information, Tsinghua University, Beijing 100084, China

³Institute for Quantum Information & State Key Laboratory of High-Performance Computing, College of Computer, National University of Defense Technology, Changsha 410073, China

⁴Center for X-ray Optics, Advanced Light Source, Lawrence Berkeley National Laboratory, Cyclotron Road, Berkeley, CA 94720, USA

⁵Department of Physics, Chonnam National University, Gwangju, 61186, Republic of Korea

⁶National Center for Electron Microscopy in Beijing, School of Materials Science and Engineering, Tsinghua University, Beijing 100084, China

*These authors contributed equally.

†Correspondence to whom should be addressed to: jiang_lab@tsinghua.edu.cn

Abstract

Interfacially asymmetric magnetic multilayers made of heavy metal/ferromagnet have attracted considerable attention in the spintronics community for accommodating spin-orbit torques and meanwhile for hosting chiral spin textures. In these multilayers,

the accompanied interfacial Dzyaloshinskii-Moriya interaction (iDMI) permits the formation of Néel-type spin textures. While significant progresses have been made in Co, CoFeB, Co₂FeAl, CoFeGd based multilayers, it would be intriguing to identify new magnetic multilayers which could enable spin-torque controllability and meanwhile host nanoscale skyrmions. In this report, we first synthesize thin films made of permanent magnet SmCo₅ with perpendicular magnetic anisotropy, in which the deterministic spin-orbit torque (SOT) switching, enabled by the spin Hall effect, in Pt/SmCo₅/Ta trilayer is demonstrated. Further, we show the stabilization of room-temperature skyrmions with diameters approximately 100 nm in [Pt/SmCo₅/Ta]₁₅, together with a skyrmionium-like spin texture in [Pt/SmCo₅/Ir]₁₅ multilayers. Based on the material specific parameters, micromagnetic simulations are also carried out. Results of which confirm the presence of chiral spin textures in this new material family. Through interfacial engineering, our results thus demonstrate that rare earth permanent magnet could be a new platform for studying the interfacial chiral spintronics.

Introduction

Interfacial chiral magnetism in the heavy metal/ferromagnet (HM/FM) bilayer has attracted considerable attention in spintronics community^[1,2]. Heavy metals with strong spin-orbit interactions such as Pt, Ta, W could enable efficient manipulation of magnetization through current-induced spin-orbit torques (SOTs)^[3-5]. Additionally, the spin-orbit interaction at the dissimilar interfaces produces an interfacial Dzyaloshinskii-Moriya interaction (iDMI)^[6-9] that stabilizes Néel-type domain walls (DWs)^[10-12] and skyrmions^[13-15]. As governed by the symmetry, the current-induced SOTs act more effectively on the Néel-type spin textures^[11,16]. While significant progresses have been made in the Co^[17,18], CoFeB^[19,20], Co₂FeAl^[21,22], GdFeCo^[23,24] based multilayers, it is interesting to exploit new material systems, in which the interplay between current-induced SOTs and chiral spin textures can be comprehensively investigated.

In this report, we first synthesize thin films made of rare-earth permanent magnet of nominal composition SmCo_5 with perpendicular magnetic anisotropy (PMA). Based on which, an electric control of perpendicular magnetization vectors by the current induced SOTs, and the stabilization of nanoscale Néel-type skyrmions are subsequently demonstrated. SmCo_5 is a well-known rare-earth permanent magnet, which has been widely investigated for the ultrahigh density recording media due to its large magnetic anisotropy. For accommodating SOTs and Néel-type skyrmions, SmCo_5 films are required to exhibit PMA. Previous studies have shown that SmCo_5 films with PMA can be obtained by epitaxially growing SmCo_5 (001) on top of Cu (111)^[25,26]. Since Cu exhibits a negligible spin-orbit coupling^[27,28], it is thus not ideal for accommodating both SOT and iDMI. In the present work, through synthesizing Pt/ SmCo_5 /N (N denotes a different HM layer) trilayers, the presence of PMA in SmCo_5 film is established through interfacial engineering. The SOT-induced deterministic magnetization switching is also demonstrated by exploiting the spin Hall effects from the involved HM layer^[3,29]. We further prepare $[\text{Pt}/\text{SmCo}_5/\text{N}]_{15}$ (N = Ta, W and Ir) multilayers, in which the formation of nanoscale skyrmions and skyrmionium-like spin textures are experimentally and numerically studied. Our work demonstrates that rare earth permanent magnet SmCo_5 could largely expand the material choice for interfacial chiral spintronics.

Results and discussion

Schematic illustration of the SmCo_5 based asymmetric magnetic multilayer is shown in Fig. 1(a). In particular, Ta(1)/Pt(3)/ $\text{SmCo}_5(t)$ /N(3) multilayers (thickness in nm, with N = Ta, W, Ir) are deposited by using an ultrahigh vacuum sputtering system. Particularly, for the SmCo_5 film deposition, a commercially available SmCo_5 compound target is used. In order to characterize the composition of SmCo_5 film, we carried out an X-ray photoelectron spectroscopy (XPS) measurement in the energy range of 750-1200 eV, as shown in Fig. 1(b). From the Sm 3d spectrum, two peaks

appear at 1110.4 eV and 1083 eV, corresponding to Sm $3d_{3/2}$ and $3d_{5/2}$, respectively. The other two peaks are located at 792.7 eV and 777.5 eV, which correspond to Co $2p_{1/2}$ and Co $2p_{3/2}$, respectively. This result confirms the presence of Sm and Co elements. Through dividing the integrated element intensity by the element sensitivity from the XPS measurement, the Sm/Co atomic ratio can be approximately determined to be 1/4.67, which is close to the nominal composition of the sputtering target. Note that the atomic ratio of Sm/Co (1/4.77) is further confirmed through performing an Energy-dispersive X-ray spectroscopy (EDS) experiment, as shown in the Supplementary Information.

The magnetic properties of Pt/SmCo₅/Ta trilayers are studied using a superconducting quantum interference device (SQUID) magnetometer. Shown in Figs. 1(c) and 1(d) are the magnetic hysteresis loops ($M-H$) that are acquired in films with different thicknesses (t) of SmCo₅, with fields being applied perpendicular (H_z) and parallel ($H_{//}$) to the film plane, respectively. When $t < 1.2$ nm, the Pt/SmCo₅/Ta trilayers exhibit an in-plane anisotropy. Following the increased thickness of SmCo₅ films to $t=1.5$ nm, a square-like hysteresis loop ($M-H_z$) confirms the presence of PMA. Values of the saturation magnetization (M_s) and the PMA effective field ($\mu_0 H_k$) are also extracted and shown in Figs. 1(e) and 1(f), respectively. The value of $\mu_0 H_k$ increases with the increase of thickness ($t < 1.5$ nm), and followed by a decrease of $\mu_0 H_k$ for $t > 1.5$ nm. Thus, we can identify the strongest PMA of value $\mu_0 H_k = 400$ mT at $t = 1.5$ nm. Considering the strong thickness dependent magnetic anisotropy, our results thus suggest that the occurrence of PMA in the Pt/SmCo₅/Ta based trilayer is of interfacial origin. This observation could be related to the orbital hybridization between the $5d$ transition metal Pt and SmCo₅, similar to that of Pt/Co interface^[30,31].

Since the strongest PMA is observed in Pt/SmCo₅(1.5 nm)/Ta trilayer, we use this thickness to study the current-induced SOTs, the existence of noncollinear spin textures and most importantly their interplay in the subsequent studies. Note that the

magnetic damping parameters $\alpha=0.31$ for Pt/SmCo₅/Ta, $\alpha=0.31$ for Pt/SmCo₅/W, and $\alpha=0.19$ for Pt/SmCo₅/Ir were respectively obtained through analyzing the symmetric and antisymmetric components of the spectra acquired from spin-torque ferromagnetic resonance (ST-FMR) experiments^[32], as shown in the Supplementary Information. Note that the relatively large damping parameters can be minimized through an annealing process.

The incorporation of a Pt layer not only helps the development of PMA, but also permits the current-induced SOT manipulation of the Pt/SmCo₅/Ta trilayer, through the electronic spin Hall effect^[33,34], as shown in Fig. 2(a). Note that the deposition of Pt and Ta layers on the opposite surfaces of SmCo₅ film is motivated by the opposite spin Hall angles of Pt and Ta^[28]. This results in additive SOTs acting on the SmCo₅^[35], which can be beneficial for efficient perpendicular magnetization switching. An optical image of the typical Hall-bar device is shown in Fig. 2 (b). The current-induced SOT switching in the presence of in-plane fields ($\mu_0 H_x$) is performed in the Hall geometry, as shown in Figs. 2(c) and 2(d), respectively. Through applying both the current density (J_c) and in-plane fields ($\mu_0 H_x$) along the x direction, the anomalous Hall effect (AHE) resistance (R_{xy}) is monitored. Since R_{xy} is proportional to the perpendicular magnetization (M_z)^[36], the reversal of R_{xy} thus reflects the reversal of M_z .

In the presence of $\mu_0 H_x = \pm 100$ mT, upon sweeping J_c , the AHE loops change their polarities depending on the direction of $\mu_0 H_x$, signifying the current-induced SOT switching of the perpendicular magnetization (M_z). This is consistent with the reversed direction of the damping-like SOT effective field, which is a typical feature of the SOT-induced magnetization switching in similar PMA films^[3,33]. A “diamond-shaped” switching phase diagram is summarized in Fig. 2(e), in which the dependence of critical switching current density ($\pm J_{th}$) on the in-plane fields ($\pm \mu_0 H_x$) can be clearly seen. The critical switching current density J_{th} changes from 1.04×10^7 A/cm² to 0.67×10^7 A/cm², as $\mu_0 H_x$ increases from 10 mT to 130 mT. This observation can

be attributed to the fact that the larger tilting of M_z from out of plane results in a reduction of energy barrier and hence a decreased J_{th} . Our results thus demonstrate that the complementary SOTs in the Pt/SmCo₅/Ta trilayer can be implemented to electrically manipulate the perpendicular magnetization of the SmCo₅ films.

We further studied the evolution of PMA in Pt/SmCo₅/N trilayers. Shown in Figs. 3(a) and 3(b) are the $M-H$ loops obtained in Pt/SmCo₅/N (N = Ta, W and Ir) trilayers with magnetic fields being applied out-of-plane (H_z) and in-plane ($H_{//}$), respectively. With the thickness of SmCo₅ layer being fixed at 1.5 nm, it is clear that different capping layers strongly modulate the strength of PMA. Namely, following the increase of atomic number from Ta, W to Ir, the strength of PMA in Pt/SmCo₅/N gradually decreases^[37,38].

In order to simultaneously quantify the efficiency of the current-induced SOTs and the evolution of iDMI in these trilayers, we carry out a spin Hall magnetometry experiment. By applying a *dc* current into Pt/SmCo₅/N trilayers, the SOT effective field can be written as^[39,40]:

$$H_{eff}^z = \frac{\hbar \theta_{sh} j_e}{2 e \mu_0 M_s t_F} \cos \Phi(j_e, \vec{m}), \quad (1)$$

here, \hbar , θ_{sh} , j_e , e , μ_0 , M_s , t_F are the reduced Planck constant, the spin Hall angle of the HM, the charge current density flowing in the HM, the elementary charge, the vacuum permeability, the saturation magnetization and the thickness of the magnetic film, respectively. And \vec{m} is the spin orientation in the center of DWs which determines the DW of being (chiral/achiral) Néel/Bloch types, $\Phi(j_e, \vec{m})$ is the relative angle between j_e and \vec{m} . In the case of j_e and \vec{m} are collinear^[39,40], $\cos \Phi = \pm 1$. This corresponds to the motion of chiral Néel-type of DW. Through applying in-plane magnetic fields ($H_{x,y}$) which compete with the effective field of iDMI (H_D), spins inside the DW (\vec{m}) start to rotate, which alter the magnitude of H_{eff}^z . As a result, dynamics of DW driven by j_e change from motion ($|H_x| < H_D$) to contraction or expansion ($|H_x| > H_D$). In particular, the SOT efficiency of $\chi_{SOT} = \mu_0 H_{eff}^z / j_e$ will be saturated when the DW

profile changes from chiral to achiral Néel DWs (at which H_x fully compensates H_D). Thus χ_{SOT} enables both the effective field of iDMI and the efficiency of SOTs to be simultaneously obtained.

Since H_{eff}^z can be treated as an effective field along the z-axis, the presence of H_{eff}^z manifests as a horizontal shift of AHE loop in the presence of $\pm\mu_0 H_x$ and $\pm j_e$. Shown in Fig. 3(c) are typical results of spin Hall magnetometry, measured in a Pt/SmCo₅/Ta trilayer with $\mu_0 H_x = +50$ mT and $I = \pm 6$ mA. The distinct horizontal shift of the AHE loops from the origin can be clearly seen. In particular, the effective field $\mu_0 H_{eff}^z = i$ can be determined, in which $\mu_0 \Delta H^{+ii}$ ($\mu_0 \Delta H^{-ii}$) denotes the shift of AHE loops from the origin in the presence of $I = 6$ mA ($I = -6$ mA), respectively. [The shifted loops for Pt/SmCo₅/W and Pt/SmCo₅/Ir trilayers were given in the Supplementary Information.](#) Through systematically examining the dependence of $\mu_0 H_{eff}^z$ on $\mu_0 H_x$, a SOT efficiency χ_{SOT} vs. H_x can be obtained, as shown in Fig. 3(d).

It has been mentioned that the saturation of χ_{SOT} vs. H_x corresponds to the compensation of H_D by H_x (*i.e.*, Néel DWs from being chiral to achiral)^[39,41]. This enables the effective field of iDMI (H_D) to be directly determined. It is known that the iDMI parameter $D = \mu_0 M_s \Delta H_D$, where $\Delta = \sqrt{2A/\mu_0 M_s H_k}$ is the DW width and A is exchange stiffness coefficient^[39,40], respectively. Following a simple calculation, the iDMI parameters for Pt/SmCo₅/N trilayers (N = Ta, W, Ir) are estimated to be 1.47 mJ/m², 1.35 mJ/m² and 0.75 mJ/m², respectively. Such a decrease of iDMI following the increase of atomic number (Ta, W and Ir) shares a similar trend as the evolution of PMA strength. This observation indicates the important role of spin-orbit interaction in mediating PMA and iDMI in the present material system. These parameters are tabulated in Table 1. Note that the evolution of iDMI in Pt/SmCo₅/Ta (W, Ir) trilayers is in stark contrast with that of Pt/Co/Ta (W, Ir) trilayers^[15,42,43], in which the additive iDMI is maximized in the Pt/Co/Ir trilayer. This observation can be linked to the

usage of SmCo₅ that modifies the spin-orbit interaction energy at the interface and hence the strength of iDMI, as well as the PMA. On the other hand, a clear understanding of this aspect requires further studies from the first principle calculation.

The efficiency χ_{SOT} in these Pt/SmCo₅/N trilayers are also examined. It should mention here that efficiencies χ_{SOT} in Pt/SmCo/Ta and Pt/SmCo₅/W trilayers are larger than that in Pt/SmCo₅/Ir trilayer. We attribute this observation to the negligible spin Hall effect in Ir and the additive SOTs arising from the opposite spin Hall angles

between Pt and Ta (or W)^[44,45]. Based on $\theta_{SH} = \frac{2e}{\hbar} M_s t_F \chi$, the effective spin Hall angles of Pt/SmCo₅/Ta, Pt/SmCo₅/W and Pt/SmCo₅/Ir can be obtained as 0.68, 0.53 and 0.29, respectively. These values are in agreement with the sum of the reported spin Hall angles of Pt (+0.02~0.15)^[28,46], Ta (-0.15~-0.25)^[47,48], W (-0.18~-0.36)^{45, [49]}, and Ir (0.01~0.02)^[50,51] films, and are similar with the results from the Pt/Co/Ta^[44] and W/CoTb/Pt^[45] trilayers.

The relatively large iDMI strengths in Pt/SmCo₅/N trilayers suggest the possible formation of Néel-type spin textures in SmCo₅ based inversion asymmetric multilayers. We subsequently synthesize Ta/[Pt/SmCo₅/N]₁₅/Ta (N = Ta, W, Ir) multilayers. Shown in Fig. 4(a) are the perpendicular magnetic hysteresis loops ($M-H_z$), following the order of Ta, W and Ir, respectively. Note that these loops are similar to those of typical multilayers hosting skyrmions^[52-54].

To observe the formation of nanoscale skyrmions and their field-driven dynamics in Ta/[Pt/SmCo₅/N]₁₅/Ta (N = Ta, W, Ir) multilayers, we performed a magnetic transmission soft X-ray microscopy experiment on multilayers grown on 100 nm thick Si₃N₄ membranes, at the Co L₃ edge. Shown in Figs. 4(b) - 4(d) are the X-ray magnetic circular dichroism (XMCD) images acquired in Ta/[Pt/SmCo₅/Ta]₁₅/Ta multilayer at

$\mu_0 H_z = 45$ mT (marked as I), $\mu_0 H_z = 0$ mT (marked as II) and $\mu_0 H_z = -30$ mT (marked as III), respectively. These images also correspond to the marked red points in Fig. 4(a). It is clear that bubble-like spin textures are observed at high magnetic fields (I and III), while labyrinthine domains emerge at zero field (II). The corresponding XMCD images for Ta/[Pt/SmCo₅/W]₁₅/Ta and Ta/[Pt/SmCo₅/Ir]₁₅/Ta multilayer are shown in Figs. 4(f) - 4(h) and Figs. 4(j) - 4(l), respectively. At zero magnetic field, it can be seen that the domain width increases following the order of Ta, W and Ir, reflecting the decrease of iDMI. More interestingly, we observed a skyrmionium-like spin textures in the Ta/[Pt/SmCo₅/Ir]₁₅/Ta multilayer.

In order to reveal the detailed spin profile of these noncollinear spin textures, we subsequently performed a layer-resolved micromagnetic simulations based on the material specific parameters that were tabulated in Table 1. The micromagnetic simulation at $\mu_0 H_z = 50$ mT is done by using the Mumax3 software, results of which are shown in Fig. 5 for [Pt/SmCo₅/Ta]₁₅, [Pt/SmCo₅/W]₁₅ and [Pt/SmCo₅/Ir]₁₅, respectively. The top view of the spin profiles shown in the left column, corresponding to a single isolated skyrmion, stripe domains and a skyrmionium that were found in the [Pt/SmCo₅/Ta]₁₅, [Pt/SmCo₅/W]₁₅ and [Pt/SmCo₅/Ir]₁₅ multilayers, respectively. The layer-resolved spin profiles can be seen from the right panels. The layer-resolved results suggest the same spin profile maintained in each magnetic layer of the [Pt/SmCo₅/Ta]₁₅ and [Pt/SmCo₅/W]₁₅ multilayers, as shown in Figs. 5 (b) and (d), respectively. The skyrmionium shown in Fig. 5 (f) in the [Pt/SmCo₅/Ir]₁₅ multilayer, however, exhibits a hybridized spin profile. **Namely, the arrangement of magnetic moments in the first three layers is opposite with the last twelve layers, which is similar to the hybridized spin textures that were observed in multilayers with relatively small iDMI^[55,56].** This is caused by the competitive effect of iDMI and interlayer dipole coupling. Namely, the Ta and W capping layers introduce relatively large iDMI values that maintain the spin chirality of each magnetic layer. However, in [Pt/SmCo₅/Ir]₁₅ multilayer, the interlayer dipole coupling overcomes the relatively small iDMI that

reverses the spin chirality of different magnetic layers, which results in the formation of hybridized skyrmionium profile across the magnetic layers.

Conclusion

In conclusion, based on the rare earth permanent magnet SmCo_5 , we have investigated the thickness and interface dependent PMA in a series of $\text{Pt}/\text{SmCo}_5/\text{N}$ ($\text{N} = \text{Ta}, \text{W}$ and Ir) trilayers. In particular, we have identified an interfacial origin of the PMA, and we have also found that the $\text{Pt}/\text{SmCo}_5(1.5 \text{ nm})/\text{Ta}$ trilayer exhibits the strongest PMA. We further investigated the current-induced SOT switching, the efficiency of spin-orbit torques and iDMI in the $\text{Pt}/\text{SmCo}_5/\text{N}$ ($\text{N} = \text{Ta}, \text{W}, \text{Ir}$) trilayers. We have found that both the strength of PMA and interfacial DMI are strongest with Ta capping which decrease following the increase of atomic number to W and to Ir. Our results thus identified the important role of spin-orbit interaction in mediating PMA, SOTs and iDMI in the present material system. Through synthesizing magnetic multilayers $[\text{Pt}/\text{SmCo}_5/\text{N}]_{15}$ ($\text{N} = \text{Ta}, \text{W}$ and Ir), the stabilization of skyrmions around 100 nm is identified by using the transmission X-ray microscopy. More intriguingly, a skyrmionium-like spin texture is experimentally discovered. Through using the material specific parameters, we carried out layer-resolved micromagnetic simulations, which reveals the detailed spin profile of these noncollinear spin textures. In the future, one could optimize the growth conditions of SmCo_5 for achieving a stronger perpendicular magnetic anisotropy, which could be beneficial for realizing thermally stable SOT devices and smaller skyrmions. Nevertheless, our results demonstrate that the rare earth permanent magnet could be implemented for optimizing the interaction between spin-orbit torques and noncollinear spin textures, which can be useful for the future development of interfacial chiral spintronics.

Experiments

SmCo_5 films with varying thicknesses were deposited via the dc magnetron sputtering from a SmCo_5 compound target (purity 99.95%) at room temperature by using an

ultrahigh vacuum (UHV) sputtering system (AJA-Orion 8). The base pressure of the main chamber is better than 2×10^{-8} Torr. During the deposition, the argon pressure was fixed at 3 mTorr and depositing rate of each layer is 0.02 nm/s. We prepared Ta(1 nm)/Pt(3 nm)/SmCo₅(*t* nm)/N(3 nm) and Ta(1 nm)/[Pt(3 nm)/SmCo₅(1.5 nm)/N(3 nm)]₁₅ multilayers in which N denotes different capping layers such as Ta, W and Ir (thickness in nm). A 1 nm Ta seeding layer is deposited before growing Pt layer. A 3 nm capping layer is used to maintain asymmetric interfaces and meanwhile acts as a protection layer. Films grown on the Si/SiO₂ substrates were used for magnetometry and transport measurements. X-ray photoelectron spectroscopy (XPS) analysis was carried out by using an Escalab-250 instrument (Thermo Fisher Scientific, USA) that is equipped with a hemisphere detector and a monochromatic Al-K α X-ray source. [The Energy-dispersive X-ray spectroscopy \(EDS\) analysis was carried out by using high performance field emission scanning electron microscope \(Zeiss Merlin\).](#) Magnetometry measurements were done using a superconducting quantum interference device (SQUID) magnetometer. Hall-bar devices were fabricated by standard photolithography and followed by an argon ion milling process. The current-induced SOT switching and spin Hall magnetometry measurements were done using a triple-axis superconducting magnet (5T-2T-2T). The multilayers were grown on 100 nm thickness Si₃N₄ membrane (Clean SiN, Suzhou). The X-ray magnetic circular dichroism (XMCD) imaging in transmission geometry were done at the Co L₃ edge (778.5 eV) using a full-field transmission soft X-ray microscope (XM-1) at the beamline 6.1.2 at the Advanced Light Source of Lawrence Berkeley National Laboratory. In order to probe the out-of-plane XMCD contrast, samples were positioned with the plane normal in parallel with the incident circularly polarized X-ray beam.

Micromagnetic Simulations

The micromagnetic simulations were performed by means of numerically integrating the Landau–Lifshitz–Gilbert equation using the Mumax3 software:

$$\frac{d\vec{M}}{dt} = -\gamma \vec{M} \times \vec{H}_{eff} - \frac{\alpha\gamma}{M_s} [\vec{M} \times (\vec{M} \times \vec{H}_{eff})], \quad (e-1)$$

where α is the damping coefficient, \vec{M} is the magnetization vector, M_s is the saturation magnetization, γ is the gyromagnetic ratio, and $\vec{H}_{eff} = -\frac{1}{\mu_0 V} \frac{dE}{d\vec{M}}$ is the effective field generated by energies (DMI energy, Zeeman energy, exchange energy, interlayer dipole coupling energy, magnetic anisotropy energy and demagnetization energy). Here, $\mu_0 = 4\pi \times 10^{-7} T \cdot m/A$ is the vacuum permeability and V is the volume of each element. We used a discretization cell of $2 \times 2 \times 1.5 \text{ nm}^3$ for $[\text{Pt}/\text{SmCo}_5/\text{Ta}]_{15}$ multilayer, $5 \times 5 \times 1.5 \text{ nm}^3$ for $[\text{Pt}/\text{SmCo}_5/\text{W}]_{15}$ and $[\text{Pt}/\text{SmCo}_5/\text{Ir}]_{15}$ multilayers, with the specific parameters tabulated in the Table 1. The exchange constant $A = 10 \text{ pJ/m}$ and the perpendicular magnetic field is at $H_z = 50 \text{ mT}$, respectively.

Acknowledgements:

Work carried out at Tsinghua was supported by the Basic Science Center Project of NSFC (Grant No. 51788104), the National Key R&D Program of China (Grant Nos. 2017YFA020620, 2016YFA03023000), the National Natural Science Foundation of China (Grant No. 11774194, 11804182, 1181101082, 51831005), Beijing Natural Science Foundation (Grant No. Z190009), and the Beijing Advanced Innovation Center for Future Chip (ICFC). Works at the ALS were supported by U.S. Department of Energy (DE-AC02-05CH11231). S.J. is supported by the National Research Foundation of Korea (NRF) grant funded by the Korea government (MSIT) (No. 2020R1C1C1006194). M.-Y.I. acknowledges support by Lawrence Berkeley National Laboratory through the Laboratory Directed Research and Development (LDRD) Program.

Author contributions

W.J., H.Z. conceived the idea and designed the experiments. H.Z., T.X. and L.Z. fabricated the thin film, H.Z., Q.Z. and Y.D. did the transport and magnetometry measurements. Z.W., S.J., M.I and W.J. performed the full field soft X-ray

microscope imaging experiments. J.L. performed micromagnetic simulation. [K.X.](#) and [J.Z.](#) did the EDS experiment. W.J. wrote the manuscript with inputs from all authors.

Additional information.

Supplementary information is available in the online version of the paper. Preprints and permission information is available online. Correspondence and requests for materials should be addressed to W.J.

Availability of data

The data that support the findings of this study are available from the corresponding author upon reasonable request.

Competing financial interests

Authors declare no competing financial interests.

References:

- [1] A. Soumyanarayanan, N. Reyren, A. Fert, and C. Panagopoulos, *Nature* **539**, 509 (2016).
- [2] F. Hellman, A. Hoffmann, Y. Tserkovnyak, G. S. D. Beach, E. E. Fullerton, C. Leighton, A. H. MacDonald, D. C. Ralph, D. A. Arena, H. A. Dürr, P. Fischer, J. Grollier, J. P. Heremans, T. Jungwirth, A. V. Kimel, B. Koopmans, I. N. Krivorotov, S. J. May, A. K. Petford-Long, J. M. Rondinelli, N. Samarth, I. K. Schuller, A. N. Slavin, M. D. Stiles, O. Tchernyshyov, A. Thiaville, and B. L. Zink, *Review of modern physics* **89**, 025006 (2017).
- [3] L. Liu, C.-F. Pai, Y. Li, H. W. Tseng, D. C. Ralph, and R. A. Buhrman, *Science* **336**, 555 (2012).
- [4] K. Garello, I. M. Miron, C. O. Avci, F. Freimuth, Y. Mokrousov, S. Blugel, S. Auffret, O. Boulle, G. Gaudin, and P. Gambardella, *Nat. Nanotechnol.* **8**, 587 (2013).
- [5] A. Manchon, J. Železný, I. M. Miron, T. Jungwirth, J. Sinova, A. Thiaville, K. Garello, and P. Gambardella, *Rev. Mod. Phys.* **91**, 035004 (2019).
- [6] A. Crépieux and C. Lacroix, *J. Magn. Magn. Mater.* **182**, 341 (1998).
- [7] H. Yang, A. Thiaville, S. Rohart, A. Fert, and M. Chshiev, *Phys. Rev. Lett.* **115**, 267210 (2015).

- [8] S. Karayev, P. D. Murray, D. Khadka, T. R. Thapaliya, K. Liu, and S. X. Huang, *Phys. Rev. Mater.* **3**, 041401(R) (2019).
- [9] A. Fert, V. Cros, and J. Sampaio, *Nat Nanotechnol* **8**, 152 (2013).
- [10] M. Heide, G. Bihlmayer, and S. Blügel, *Phys. Rev. B* **78**, 140403(R) (2008).
- [11] S. Emori, U. Bauer, S. M. Ahn, E. Martinez, and G. S. Beach, *Nat. Mater.* **12**, 611 (2013).
- [12] K.-S. Ryu, L. Thomas, S.-H. Yang, and S. Parkin, *Nat. Nanotechnol.* **8**, 527 (2013).
- [13] W. Jiang, P. Upadhyaya, W. Zhang, G. Yu, M. B. Jungfleisch, F. Y. Fradin, J. E. Pearson, Y. Tserkovnyak, K. L. Wang, O. Heinonen, S. G. E. te Velthuis, and A. Hoffmann, *Science* **349**, 283 (2015).
- [14] S. Woo, K. Litzius, B. Kruger, M. Y. Im, L. Caretta, K. Richter, M. Mann, A. Krone, R. M. Reeve, M. Weigand, P. Agrawal, I. Lemesch, M. A. Mawass, P. Fischer, M. Klaui, and G. S. Beach, *Nat. Mater.* **15**, 501 (2016).
- [15] C. Moreau-Luchaire, S. C. Mouta, N. Reyren, J. Sampaio, C. A. Vaz, N. Van Horne, K. Bouzehouane, K. Garcia, C. Deranlot, P. Warnicke, P. Wohlhuter, J. M. George, M. Weigand, J. Raabe, V. Cros, and A. Fert, *Nat. Nanotechnol.* **11**, 444 (2016).
- [16] S.-G. Je, D.-H. Kim, S.-C. Yoo, B.-C. Min, K.-J. Lee, and S.-B. Choe, *Phys. Rev. B* **88**, 214401 (2013).
- [17] L. Wang, C. Liu, N. Mehmood, G. Han, Y. Wang, X. Xu, C. Feng, Z. Hou, Y. Peng, X. Gao, and G. Yu, *ACS Appl Mater Interfaces* **11**, 12098 (2019).
- [18] D. Bhattacharya, S. A. Razavi, H. Wu, B. Dai, K. L. Wang, and J. Atulasimha, *Nat. Electron.* **3**, 539 (2020).
- [19] G. Yu, P. Upadhyaya, X. Li, W. Li, S. K. Kim, Y. Fan, K. L. Wong, Y. Tserkovnyak, P. K. Amiri, and K. L. Wang, *Nano Lett.* **16**, 1981 (2016).
- [20] W. Jiang, G. Chen, K. Liu, J. Zang, S. G. E. te Velthuis, and A. Hoffmann, *Phys. Rep.* **704**, 1 (2017).
- [21] W. Akhtar, A. Hrabec, S. Chouaieb, A. Haykal, I. Gross, M. Belmeguenai, M. S. Gabor, B. Shields, P. Maletinsky, A. Thiaville, S. Rohart, and V. Jacques, *Phys. Rev. Appl.* **11**, 034066 (2019).
- [22] C. He, A. Razavi, J. Wei, H. Xu, G. Yu, K. L. Wong, H. Wu, S. Shen, Q. Chen, Z. Zeng, S. Wang, and K. L. Wang, *Appl. Phys. Lett.* **117**, 172406 (2020).
- [23] S. Woo, K. M. Song, X. Zhang, Y. Zhou, M. Ezawa, X. Liu, S. Finizio, J. Raabe, N. J. Lee, S. I. Kim, S. Y. Park, Y. Kim, J. Y. Kim, D. Lee, O. Lee, J. W. Choi, B. C. Min, H. C. Koo, and J. Chang, *Nat. Commun.* **9**, 959 (2018).
- [24] K. M. Song, J.-S. Jeong, B. Pan, X. Zhang, J. Xia, S. Cha, T.-E. Park, K. Kim, S. Finizio, J. Raabe, J. Chang, Y. Zhou, W. Zhao, W. Kang, H. Ju, and S. Woo, *Nat. Electron.* **3**, 148 (2020).
- [25] J. Sayama, K. Mizutani, T. Asahi, J. Ariake, K. Ouchi, and T. Osaka, *J. Magn. Magn. Mater.* **301**, 271 (2006).
- [26] M. Seifert, V. Neu, and L. Schultz, *Appl. Phys. Lett.* **94**, 022501 (2009).
- [27] T. M. Dunn, *Transactions of the Faraday Society* **57**, 1441 (1961).

- [28] H. L. Wang, C. H. Du, Y. Pu, R. Adur, P. C. Hammel, and F. Y. Yang, *Phys. Rev. Lett.* **112**, 197201 (2014).
- [29] G. Yu, P. Upadhyaya, K. L. Wong, W. Jiang, J. G. Alzate, J. Tang, P. K. Amiri, and K. L. Wang, *Phys. Rev. B* **89**, 104421 (2014).
- [30] P. F. Carcia, A. D. Meinhaldt, and A. Suna, *Appl. Phys. Lett.* **47**, 178 (1985).
- [31] P. F. Carcia, *J. Appl. Phys.* **63**, 5066 (1988).
- [32] L. Liu, T. Moriyama, D. C. Ralph, and R. A. Buhrman, *Phys. Rev. Lett.* **106**, 036601 (2011).
- [33] L. Liu, O. J. Lee, T. J. Gudmundsen, D. C. Ralph, and R. A. Buhrman, *Phys. Rev. Lett.* **109**, 096602 (2012).
- [34] J. Sinova, S. O. Valenzuela, J. Wunderlich, C. Ô. Back, and T. Jungwirth, *Rev. Mod. Phys.* **87**, 1213 (2015).
- [35] S. Woo, M. Mann, A. J. Tan, L. Caretta, and G. S. D. Beach, *Appl. Phys. Lett.* **105**, 212404 (2014).
- [36] N. Nagaosa, J. Sinova, S. Onoda, A. H. MacDonald, and N. P. Ong, *Rev. Mod. Phys.* **82**, 1539 (2010).
- [37] M. Belmeguenai, Y. Roussigné, S. M. Chérif, A. Stashkevich, T. Petrisor, M. Nasui, and M. S. Gabor, *J. Phys. D: Appl. Phys.* **52**, 125002 (2019).
- [38] S. Peng, D. Zhu, J. Zhou, B. Zhang, A. Cao, M. Wang, W. Cai, K. Cao, and W. Zhao, *Adv. Electron. Mater.* **5**, 1900134 (2019).
- [39] C.-F. Pai, M. Mann, A. J. Tan, and G. S. D. Beach, *Phys. Rev. B* **93**, 144409 (2016).
- [40] S. Emori, E. Martinez, K.-J. Lee, H.-W. Lee, U. Bauer, S.-M. Ahn, P. Agrawal, D. C. Bono, and G. S. D. Beach, *Phys. Rev. B* **90**, 184427 (2014).
- [41] A. V. Khvalkovskiy, V. Cros, D. Apalkov, V. Nikitin, M. Krounbi, K. A. Zvezdin, A. Anane, J. Grollier, and A. Fert, *Phys. Rev. B* **87**, 020402(R) (2013).
- [42] D.-S. Han, N.-H. Kim, J.-S. Kim, Y. Yin, J.-W. Koo, J. Cho, S. Lee, M. Kläui, H. J. M. Swagten, B. Koopmans, and C.-Y. You, *Nano Lett.* **16**, 4438 (2016).
- [43] D.-Y. Kim, N.-H. Kim, Y.-K. Park, M.-H. Park, J.-S. Kim, Y.-S. Nam, J. Jung, J. Cho, D.-H. Kim, J.-S. Kim, B.-C. Min, S.-B. Choe, and C.-Y. You, *Phys. Rev. B* **100**, 224419 (2019).
- [44] S. Woo, M. Mann, A. J. Tan, L. Caretta, and G. S. D. Beach, *Appl. Phys. Lett.* **105** (2014).
- [45] Z. Zheng, Y. Zhang, X. Feng, K. Zhang, J. Nan, Z. Zhang, G. Wang, J. Wang, N. Lei, D. Liu, Y. Zhang, and W. Zhao, *Phys. Rev. Appl.* **12**, 044032 (2019).
- [46] L. Ma, L. Lang, J. Kim, Z. Yuan, R. Wu, S. Zhou, and X. Qiu, *Phys. Rev. B* **98**, 224424 (2018).
- [47] Luqiao Liu, Chi-Feng Pai, Y. Li, H. W. Tseng, D. C. Ralph, and R. A. Buhrman, *Science* **336**, 555 (2012).
- [48] M. Cecot, L. Karwacki, W. Skowronski, J. Kanak, J. Wrona, A. Zywczyak, L. Yao, S. van Dijken, J. Barnas, and T. Stobiecki, *Sci Rep* **7**, 968 (2017).
- [49] W. Skowroński, Ł. Karwacki, S. Ziętek, J. Kanak, S. Łazarski, K. Grochot, T. Stobiecki, P. Kuświk, F. Stobiecki, and J. Barnaś, *Phys. Rev. Appl.* **11**, 024039 (2019).

- [50] W. Zhang, M. B. Jungfleisch, W. Jiang, J. Sklenar, F. Y. Fradin, J. E. Pearson, J. B. Ketterson, and A. Hoffmann, *J. Appl. Phys.* **117**, 172610 (2015).
- [51] T. Fache, J. C. Rojas-Sanchez, L. Badie, S. Mangin, and S. Petit-Watelot, *Phys. Rev. B* **102**, 064425 (2020).
- [52] O. Hellwig, A. Berger, J. B. Kortright, and E. E. Fullerton, *J. Magn. Magn. Mater.* **319**, 13 (2007).
- [53] S. Woo, K. Litzius, B. Krüger, M.-Y. Im, L. Caretta, K. Richter, M. Mann, A. Krone, R. M. Reeve, M. Weigand, P. Agrawal, I. Lemesch, M.-A. Mawass, P. Fischer, M. Kl \ddot{u} ni, and G. S. D. Beach, *Nat. Mater.* **15**, 501 (2016).
- [54] G. Yu, P. Upadhyaya, Q. Shao, H. Wu, G. Yin, X. Li, C. He, W. Jiang, X. Han, P. K. Amiri, and K. L. Wang, *Nano Lett.* **17**, 261 (2017).
- [55] W. Li, I. Bykova, S. Zhang, G. Yu, R. Tomasello, M. Carpentieri, Y. Liu, Y. Guang, J. Grafe, M. Weigand, D. M. Burn, G. van der Laan, T. Hesjedal, Z. Yan, J. Feng, C. Wan, J. Wei, X. Wang, X. Zhang, H. Xu, C. Guo, H. Wei, G. Finocchio, X. Han, and G. Schutz, *Adv. Mater.* **31**, 1807683 (2019).
- [56] W. Legrand, J.-Y. Chauleau, D. Maccariello, N. Reyren, S. Collin, K. Bouzehouane, N. Jaouen, V. Cros, and A. Fert, *Science Advances* **4**, eaat0415 (2018).

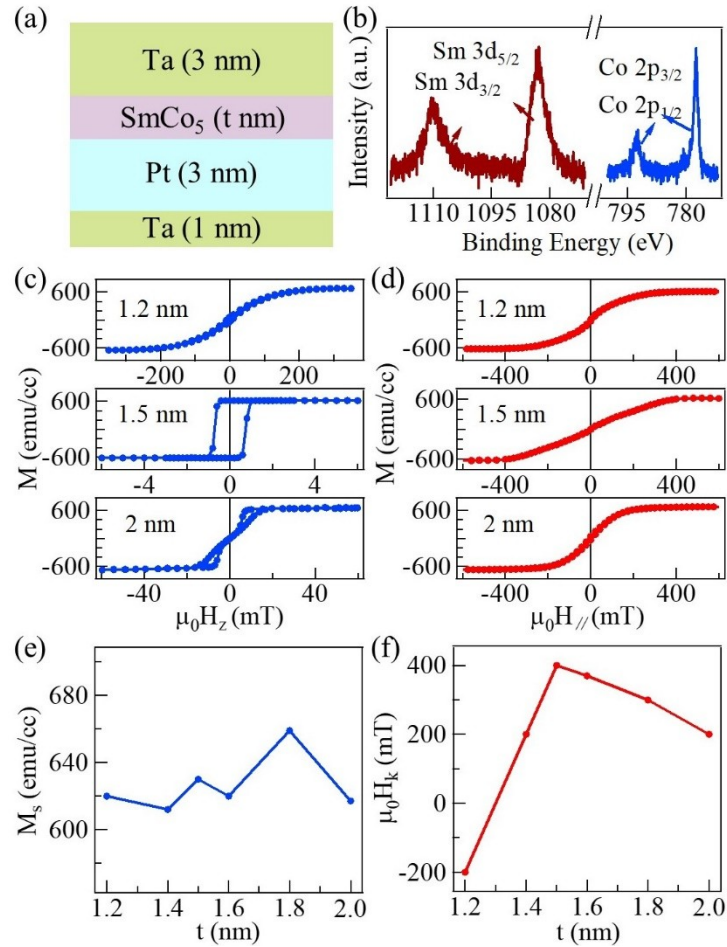


Figure 1. (a) The structure sketch of the Ta/Pt/SmCo₅/Ta multilayer. (b) The XPS spectra of Sm 3d and Co 2p. (c) and (d) The magnetic hysteresis loops of Ta/Pt/SmCo₅($t = 1.2, 1.5$ and 2 nm)/Ta multilayers measured by using SQUID with magnetic fields being applied perpendicular (H_z) and parallel ($H_{//}$) to the sample plane. (e) Thickness dependent saturation magnetization (M_s) of SmCo₅ multilayers. (f) The evolution of the perpendicular magnetic anisotropy field (H_k) as a function of the thicknesses (t) of SmCo₅.

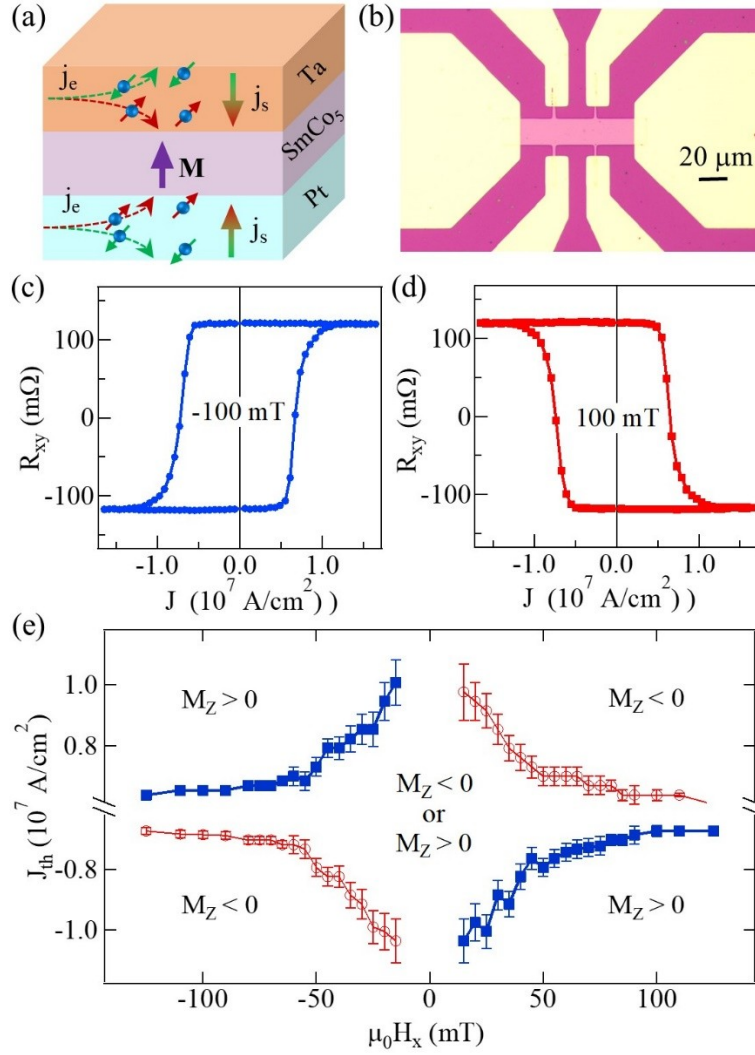


Figure 2. (a) An optical image of the fabricated Hall-bar device. (b) The sketch of spin currents generated in Pt and Ta layer via the spin Hall effect. (c) and (d) The Hall resistance with cycling current density with in-plane magnetic field $\mu_0 H_x = +100$ mT and $\mu_0 H_x = -100$ mT, respectively. (e) The switching phase diagram which summarizes the critical switching current density versus in-plane magnetic fields, $M_z > 0$ and $M_z < 0$ correspond to the normal component of the magnetization pointing up and down, respectively. The curves define the boundaries between different magnetization states.

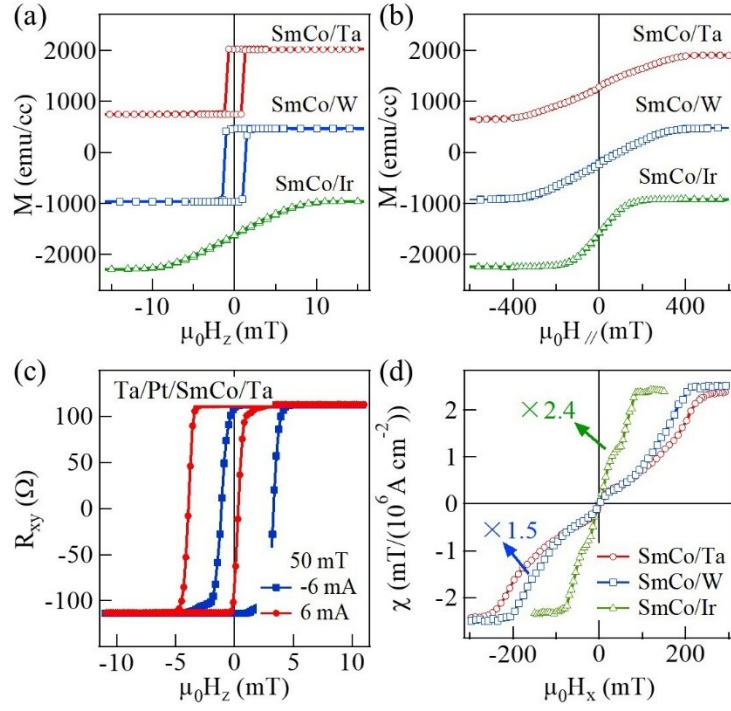


Figure 3. Shown in (a) and (b) are the hysteresis loops of Ta/Pt/SmCo₅/N (N = Ta, Ir and W) measured by SQUID with magnetic fields being applied perpendicular and parallel to the sample plane. (b) The AHE curves of Ta/Pt/SmCo₅/Ta which was measured in the Hallbar device. The distinct shift between AHE loops were observed through in the presence of $I = \pm 6 \text{ mA}$ and $\mu_0 H_x = 500 \text{ mT}$. (d) The $\mu_0 H_x$ dependent SOT efficient χ for the Ta/Pt/SmCo₅/N (N = Ta, Ir and W) multilayers.

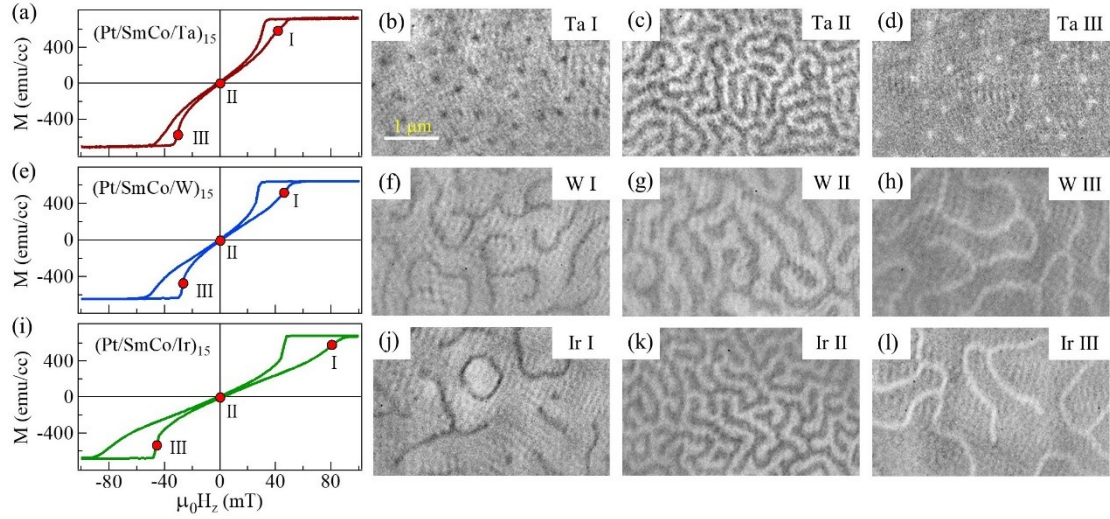


Figure 4. The hysteresis loops of the Ta/[Pt/SmCo₅/N]₁₅/Ta multilayers measured with magnetic fields being applied perpendicular to film are shown in (a), (e) and (i), with N = Ta, W, Ir. (b)-(d) The XMCD images of magnetic domain configurations in the Ta/(Pt/SmCo₅/Ta)₁₅/Ta multilayer under different magnetic fields, corresponding to the marked red points I, II and III (shown in (a)), respectively. In Fig. (b), a few isolated skyrmions show up at $\mu_0 H_z = 45$ mT. (c) Irregular domain structures are observed at zero field, (d) Changing the polarity of magnetic fields ($\mu_0 H_z = -30$ mT) reverses the magnetization orientation, and the topology of the skyrmions. (f)-(h) The XMCD images of domain states in Ta/[Pt/SmCo₅/W]₁₅/Ta multilayer under different magnetic fields, corresponding to the marked red points I (47 mT), II (0 mT) and III (-27 mT), shown in (e). (j)-(l) The XMCD images of domain states in Ta/[Pt/SmCo₅/Ir]₁₅/Ta multilayer under different magnetic fields, corresponding to the marked red points I (84 mT), II (0 mT) and III (-46 mT), shown in (i). In particular, a skyrmionium-like spin texture is identified in (j).

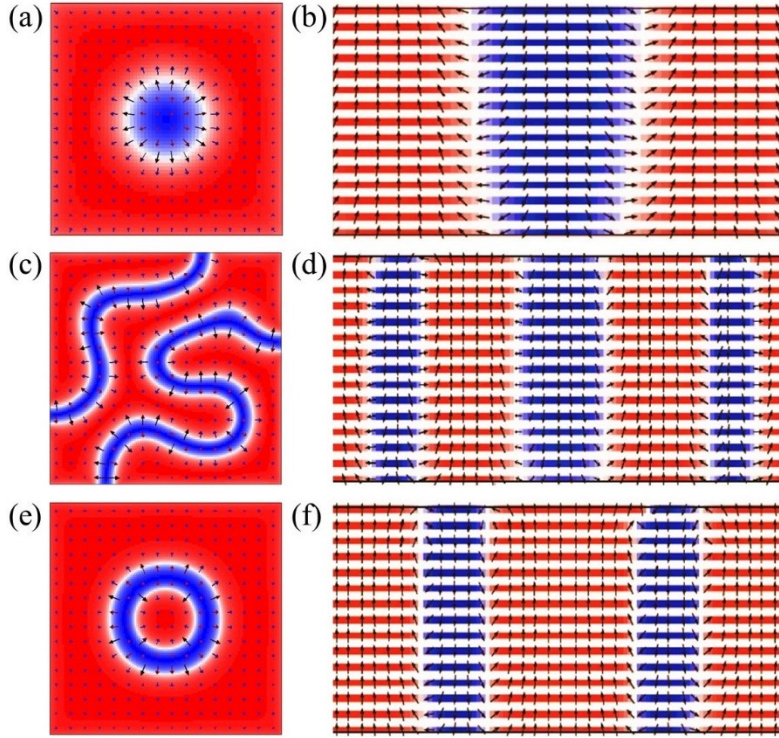


Figure 5. The layer-resolved micromagnetic simulation results based on the material specific parameters. Shown on the left/right are the top view and side view of an isolated skyrmion, stripe domains and skyrmionium that were found in $[\text{Pt}/\text{SmCo}_5/\text{Ta}]_{15}$, $[\text{Pt}/\text{SmCo}_5/\text{W}]_{15}$ and $[\text{Pt}/\text{SmCo}_5/\text{Ir}]_{15}$ multilayers, respectively. The arrows indicate the direction of the magnetization vector (m), and the different colors (from red to blue) represent the change of m_z from +1 to -1. The layer-resolved results suggest the same spin profile is maintained in each magnetic layer of the $[\text{Pt}/\text{SmCo}_5/\text{Ta}]_{15}$ and $[\text{Pt}/\text{SmCo}_5/\text{W}]_{15}$ multilayers, as shown in Figs. 5(b) and (d), respectively. The skyrmionium shown in Fig. 5 (f) in the $[\text{Pt}/\text{SmCo}_5/\text{Ir}]_{15}$ multilayer exhibits a hybridized spin profile across the magnetic layers. Namely, the configuration in first three layers is opposite with the last twelve layers.

	Trilayer						Multilayer	
	M_s (emu/cc)	$\mu_0 H_k$ (mT)	D (mJ/m ²)	χ [mT/(10 ⁶ A/cm ²)]	θ_{SH}	α	M_s (emu/cc)	$\mu_0 H_k$ (mT)
Pt/SmCo ₅ /Ta	640	380	1.47	2.38	0.68	0.31	690	130
Pt/SmCo ₅ /W	707	340	1.35	1.66	0.53	0.31	645	300
Pt/SmCo ₅ /Ir	670	160	0.75	0.99	0.29	0.19	670	180

Table 1: The material specific parameters of Pt/SmCo₅/N (N = Ta, W and Ir) trilayers and [Pt/SmCo₅/N]₁₅ multilayers.